

論文 / 著書情報
Article / Book Information

Title	Comparing vortex methods and finite difference methods in a homogeneous turbulent shear flow
Author	Rio Yokota, Shinnosuke Obi
Citation	International Journal for Numerical Methods in Fluids, Vol. 63, No. 7, pp. 828–846
Issue date	2009, 7
Copyright	This is the accepted version of the following article: International Journal for Numerical Methods in Fluids, Vol. 63, No. 7, pp. 828–846, which has been published in final form at http://dx.doi.org/10.1002/fld.2102 .
Note	このファイルは著者（最終）版です。 This file is author (final) version

Comparing vortex methods and finite difference methods in a homogeneous shear flow

R. Yokota^{*†} and S. Obi

Department of Mechanical Engineering, Keio University, 3-14-1 Hiyoshi, Kohoku-Ku, Yokohama, 223-8522, Japan

SUMMARY

The vortex method is applied to the calculation of a homogeneous shear turbulence, and compared with a finite difference code using identical calculation conditions. The core spreading method with spatial adaptation is selected as the viscous diffusion scheme of the vortex method. The shear rate is chosen so that it matches the maximum value observed in a fully developed channel flow. The isosurface, anisotropy tensors, and joint probability density functions reflect the ability of the present vortex method to quantitatively reproduce the anisotropic nature of strongly sheared turbulence, both instantaneously and statistically. Copyright © 2000 John Wiley & Sons, Ltd.

KEY WORDS: meshfree methods; finite difference methods; vortex methods; homogeneous shear flow; core spreading methods; fast multipole methods;

1. INTRODUCTION

Recent interest in vortex method studies has been focused on the development of essential tools, such as fast N-body solvers [1], high order convergent diffusion schemes [2] [3], and rigorous three-dimensional near wall treatments [4]. The maturation of each of these tools has allowed the vortex method to overcome most of its conventional weaknesses, thus making it a reliable alternative to finite difference methods for flows with a compact domain of vorticity. However, the lack of validation in canonical turbulent flows has left the overall reliability of vortex methods in question. The independent sources of errors must be investigated in simple flows, despite the fact that such flows are not always suitable for showing the advantage of vortex methods.

Like all numerical methods, vortex methods have multiple sources of numerical errors. First, even if a high order convergent diffusion scheme is used, the diffusion term calculation still contains a finite amount of error. The quantity of this error depends on the spatial resolution, the overlap ratio of vortex elements [5], and the frequency of remeshing [6], and cannot be

^{*}Correspondence to: Department of Mechanical Engineering, Keio University, 3-14-1 Hiyoshi, Kohoku-Ku, Yokohama, 223-8522, Japan

[†]E-mail: riokokota@a5.keio.jp

neglected. Another source of error is the stretching term calculation, which is highly sensitive to the spatial and temporal resolution due to its non-linearity [7]. Also, for the regions with high shear, the stretching becomes intense and the flow field becomes highly anisotropic. This may impose additional constraints on the spatial and temporal resolution [6]. It is important to determine the relation between the shear-rate and the constraints on resolution in the absence of a solid boundary. Finally, for regions near a solid boundary, a high spatial resolution in the direction normal to the wall is required. This imposes another restriction on the spatial resolution of vortex elements. It is possible to find an optimum value for the spatial resolution, temporal resolution, remeshing frequency, element anisotropy, and spatial variation of the element size if, and only if, the sources of these errors are considered independently.

There have been a few attempts to systematically investigate the independent sources of the errors mentioned above. The two-dimensional isotropic turbulence was calculated by Totsuka & Obi [8] using a vortex method and pseudo-spectral method. The rate of energy decay had good agreement with the pseudo-spectral method when spatial adaptation was implemented for their vortex method calculation. Following that, the three-dimensional isotropic turbulence was calculated by Yokota *et al.* [9] using the vortex method and pseudo-spectral method. The kinetic energy decay was in good accordance with that of the pseudo-spectral method when the spatial resolution was sufficient and spatial adaptation [5] was used. In this case, the energy spectrum matched that of the pseudo-spectral method up to the dissipation wavenumber. A related effort was made by Cottet *et al.* [10] by comparing the vortex-in-cell method to a pseudo-spectral method for the homogeneous isotropic turbulence. Their results also showed good quantitative agreement between the vortex method and pseudo-spectral method calculation, for both the decay of kinetic energy and the energy spectrum. Thus, it is fair to say that the diffusion and stretching calculation have been validated so far.

In the present study, the homogeneous shear flow is considered. A novel technique for calculating the FMM under shear periodic boundary conditions is presented. Using this technique, the vortex method calculation of the homogeneous shear flow is performed and compared with a finite difference method. The focus of this study is on the ability of vortex methods to reproduce the anisotropy of turbulence, i.e. the ability of spherical vortex blobs to reproduce streaky global vortex structures. We select a shear-rate that is comparable to the maximum shear-rate observed at $y^+ \approx 10$ in near wall flows [11]. Another objective is the assessment of the production of turbulence in vortex methods, i.e. the validation of the vortex stretching term calculation for strongly strained flows. The present calculation of the homogeneous shear flow may be considered as an intermediate validation step, which will fill the gap between the calculation of isotropic turbulence and wall bounded flows.

2. NUMERICAL METHOD

2.1. Vortex methods for homogeneous shear flows

We consider an incompressible, turbulent shear flow subject to a mean shear. In the present calculation, the instantaneous velocity and vorticity are decomposed into the time-averaged component and the fluctuating component.

$$\tilde{u}_i = U_i + u_i, \quad (1)$$

$$\tilde{\omega}_i = \Omega_i + \omega_i. \quad (2)$$

Without loss of generality, we may assume that the mean velocity is unidirectional in the downstream direction x_1 and has a constant shear-rate S in the vertical direction x_3 .

$$U_i = Sx_3\delta_{i1}. \quad (3)$$

The corresponding transport equation for the fluctuating component of vorticity can be written as

$$\frac{D\omega_i}{Dt} = \omega_j \frac{\partial u_i}{\partial x_j} + S \frac{\partial u_i}{\partial x_2} + S\omega_3\delta_{i1} + \nu \frac{\partial^2 \omega_i}{\partial x_j \partial x_j}, \quad (4)$$

where u is also the fluctuating component of velocity. The second and third term on the right hand side of Eq. (4) are the additional stretching terms, which reflect the effect of mean shear.

In the present vortex method, Eq. (4) is discretized by expressing the vorticity field as a superposition of Gaussian distributions,

$$\zeta_\sigma = \frac{1}{(2\pi\sigma^2)^{3/2}} \exp\left(-\frac{|x|^2}{2\sigma^2}\right), \quad (5)$$

where σ is the core radius of the vortex element, and $|x|$ is the distance between two vortex elements. Thus, the vorticity vector at point p is calculated by summing the influence of all particles q , each having a Gaussian distribution,

$$\omega_i^p = \sum_{q=1}^N \zeta_\sigma \alpha_i^q, \quad (6)$$

where α is the strength of the vortex element.

The velocity is calculated as the sum of the Biot-Savart velocity and the mean shear,

$$u_i^p = \sum_{q=1}^N \epsilon_{ijk} \alpha_j^q g_\sigma \frac{\partial G}{\partial x_k^q} + Sx_3^p \delta_{i1}, \quad (7)$$

where $x_i = x_i^p - x_i^q$ is the distance vector and g_σ is the cutoff function, which has the form

$$g_\sigma = \text{erf}\left(\frac{|x|}{2\sigma}\right) - \sqrt{\frac{2}{\pi}} \frac{|x|}{\sigma} \exp\left(-\frac{|x|^2}{2\sigma^2}\right). \quad (8)$$

G is the free space Green's function of the Laplace equation, and its dipole and quadrupole are

$$\frac{\partial G}{\partial x_i} = -\frac{x_i}{4\pi|x|^3}, \quad (9)$$

$$\frac{\partial^2 G}{\partial x_i \partial x_j} = -\frac{1}{4\pi} \left(\frac{\delta_{ij}}{|x|^3} - \frac{3x_i x_j}{|x|^5} \right). \quad (10)$$

Similarly, the vorticity stretching terms of Eq. (4) can be written as

$$\frac{D\alpha_i^p}{Dt} = \sum_{q=1}^N \epsilon_{ijk} \alpha_l^p \alpha_j^q \frac{\partial}{\partial x_l^p} \left(g_\sigma \frac{\partial G}{\partial x_k^q} \right) + S \epsilon_{ijk} \alpha_j^q \frac{\partial}{\partial x_2^p} \left(g_\sigma \frac{\partial G}{\partial x_k^q} \right) + S \alpha_3^p \delta_{i1}. \quad (11)$$

The diffusion term of Eq. (4) is solved by the core spreading method with spatial adaptation [9].

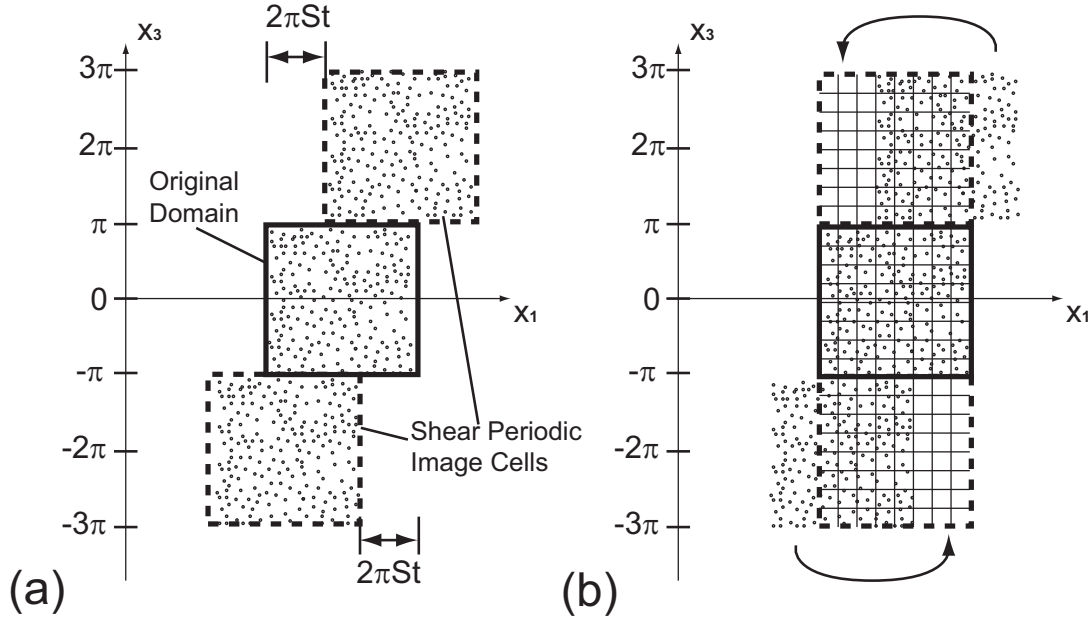


Figure 1. Schematic of element shifting in shear periodic FMM

For the calculation of Eq. (7) and Eq. (11), the shear periodic boundary condition is enforced by using a shear periodic FMM mentioned in section 2.2. Upon calculating the convection, the shear periodic boundary condition requires the elements that move out of the domain in the vertical direction x_3 to consider the shear when re-entering from the other side. For example, the elements that move out of the domain from (x_1, x_2, π) re-enter the domain from $(x_1 - 2\pi St, x_2, -\pi)$, where S is the shear-rate and t is time. The elements that move out of the domain in other directions re-enter from the opposite side by adding or subtracting 2π from the coordinates.

2.2. Shear periodic fast multipole method

The fast multipole method (FMM) has been extended to periodic boundary conditions by Lambert *et al.* [12], where the boundary condition is approximated by using a finite number of periodic images. However, to the authors' knowledge, there have been no extensions of the FMM to shear periodic boundary conditions. We introduce a novel technique to extend the FMM to shear periodic boundary conditions.

The flow of calculation of the shear periodic FMM is analogous to that of the periodic FMM. One major difference between the periodic FMM and shear periodic FMM is the treatment of periodic images in the sheared direction. In the case of a non-sheared periodic FMM, the multipole expansions for the periodic image cells are identical to that of the original cell. In other words, the periodicity of the field allows one to use the multipole expansions of the original domain to consider the contribution of the periodic images. However, for the shear periodic FMM, the multipole expansions of the periodic image cells in the sheared direction

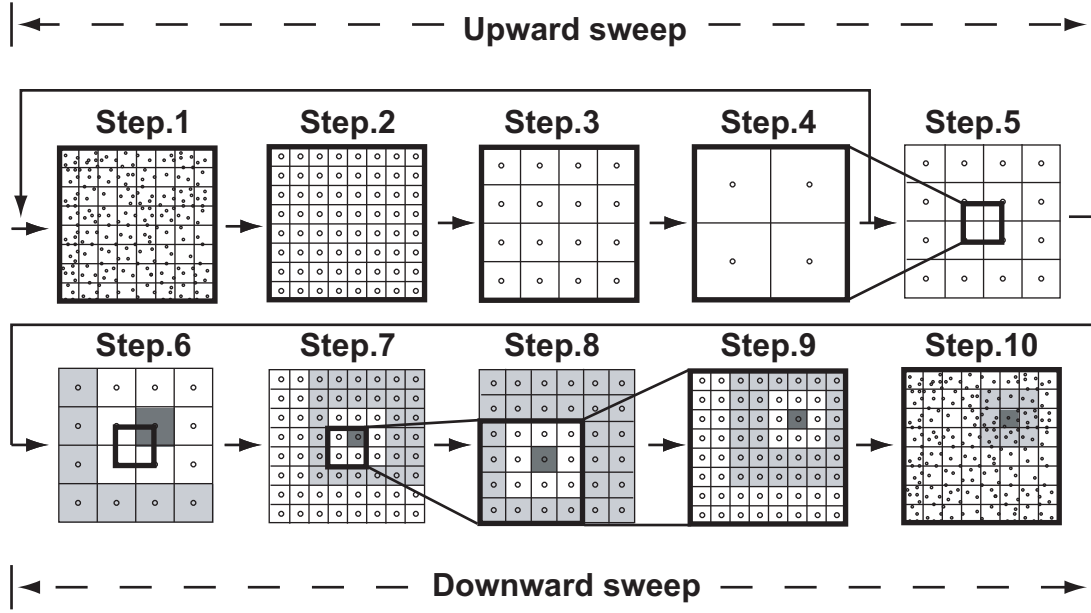


Figure 2. Flow of calculation in shear periodic FMM

are not identical to those of the original cell. We shall refer to these cells as “shear periodic image cells”.

A schematic of the shear periodic image cells is shown in Fig. 1. The solid lines represent the boundary of the original domain $[-\pi, \pi]$. The dashed lines represent the boundary of the shear periodic image cells. Figure (a) describes how the elements inside the shear periodic image cells are shifted. Figure (b) shows how the multipole expansions are calculated on an aligned cell structure. Thus, the elements that fall outside of the domain when shifted, are moved to the other side to fill the cell structure. It is necessary to calculate the multipole expansion for 2×2^k periodic image cells in the x_3 direction, each with a different shifting distance. The N th shear periodic image cell in the $\pm x_3$ direction is shifted by $\pm 2\pi NSt$.

A schematic of the flow of calculation is shown in Fig. 2. The heavy lines represent the boundary of the original domain $[-\pi, \pi]$. In step 1, the original calculation domain is repeatedly divided into smaller cells until the optimum level is reached. In step 2, the multipole expansion is calculated at the center of each cell. In steps 3 and 4, the upward sweep is performed to shift the multipole expansion to the center of the larger cells. Steps 1 through 4 are repeated for all shear periodic image cells.

In step 5, the cells are further grouped and the multipole expansions are shifted to the center of larger cells. The cells may be grouped further to account for a larger number of periodic images. In step 6, the multipole expansions are translated to local expansions for non-neighboring cells. For example, the local expansions of the dark gray cell are calculated from the multipole expansions of the light gray cells. The colored boxes are a representation of one interaction list. During the downward sweep in steps 7, 8, and 9, the cells are repeatedly divided, and the local expansions are translated to the center of these cells. At the same time,

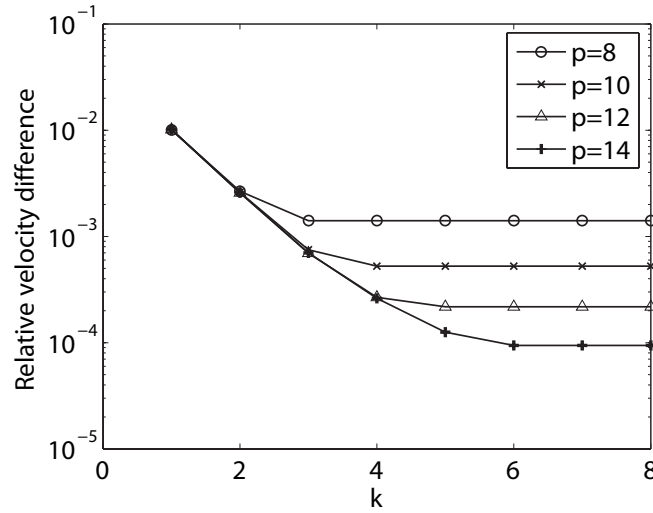
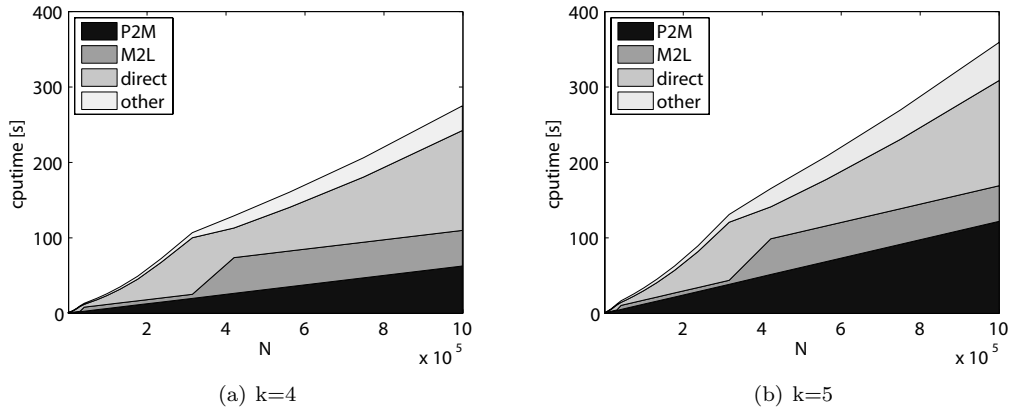


Figure 3. Relative error of the Biot-Savart calculation for a different number of shear periodic image cells

the multipole expansions of the newly non-neighboring cells (shown in light gray) are also translated to the divided cells (shown in dark gray). In step 10, the effect of the neighboring cells at the bottom level is calculated by a direct interaction of the particles. If the neighboring cell happens to be a member of the shear periodic image cell, the coordinates of the elements in the cell are accordingly shifted.

We will now examine how the number of periodic image cells and the order of the multipole expansion affect the accuracy. $N = 100$ particles with random coordinates and random strength are placed within a $[-\pi, \pi]^3$ domain and calculated for $2^k \times 2^k \times 2^k$ periodic images. The result of the direct calculation for $k = 8$ is used as a reference value. The relative velocity difference from this reference value is shown in Fig. 3, where p is the order of multipole expansions. The relative velocity difference is calculated by taking the L^2 norm of the difference from the reference value. The relative velocity difference decreases as k is increased until it reaches the accuracy limit of the FMM for the given order of multipole expansions. The results are identical to that of the periodic FMM in Yokota *et al.* [9], which is expected since shifting elements to account for the shear should not introduce additional error to the periodic FMM. For the homogeneous shear flow calculations we select $p = 10$ and $k = 4$, which have an L^2 error that is less than 10^{-3} .

The breakdown of the calculation time of the shear periodic FMM is shown in Fig. 4. Fig. 4(a) and Fig. 4(b) are the results for $k = 4$ and $k = 5$, respectively. N is the number of particles. P2M, M2L, direct, and others are the cumulative CPU-time of the particle to multipole translation, the multipole to local translation, direct summation, and everything else. The order of the multipole expansion is set to $p = 10$. For a standard periodic FMM the multipole to local translation and direct summation will take up most of the calculation time. However, since the shear periodic FMM requires the particle to multipole translation to be performed for all shear periodic image cells, its percentage rises to 25% and 30% of the total for $k = 4$ and $k = 5$, respectively.

Figure 4. Breakdown of CPU-time for Different k

In summary, the present shear periodic FMM adds no further errors to the non-shear periodic FMM, and is able to calculate at this accuracy with only a 30% increase in CPU-time.

2.3. Finite difference method

In our present calculations, the finite difference method with shear periodic boundary conditions was used as a reference [13]. When we consider the same mean shear as in Eq.(3), the Navier-Stokes equation for the fluctuating component of velocity becomes

$$\frac{\partial u_i}{\partial t} + u_j \frac{\partial u_i}{\partial x_j} + Sx_3 \frac{\partial u_i}{\partial x_1} + Su_3 \delta_{i1} = -\frac{1}{\rho} \frac{\partial p}{\partial x_i} + \nu \frac{\partial^2 u_i}{\partial x_j \partial x_j}. \quad (12)$$

This equation was solved on a staggered grid using the SMAC method. The fourth-order central difference method was used for the spatial discretization, and the third-order low storage Runge-Kutta method [15] was used for the temporal discretization.

3. HOMOGENEOUS SHEAR FLOW

The homogeneous shear flow was calculated by the vortex method and the finite difference method, using $N = 64^3, 128^3$ points. The initial Reynolds number based on Taylor's micro scale was $Re_\lambda = 25$. The calculation domain was $[-\pi, \pi]^3$ for both methods.

3.1. Initial condition

The initial conditions of the homogeneous shear flow calculation (for both the vortex method and the finite difference method) were generated from an isotropic turbulence calculation using the finite difference method. First, the initial condition for the isotropic turbulence calculation was generated in Fourier space as a solenoidal isotropic velocity field with random phases and a prescribed energy spectrum [14]. After transforming the velocity to physical space, the isotropic turbulence calculation was performed using the finite difference method until the

skewness of the velocity derivative reached a steady-state value of -0.5 . The finite difference calculation used this initial condition directly.

The initial condition for the vortex method was generated as follows. First, the vortex elements were placed on the nodes of the finite difference method grid. Then, the vorticity at the grid points was calculated from the initial velocity field using a fourth order central difference method. Following that, the strength of the vortex elements was calculated from the vorticity by using a radial basis function interpolation [5]. The BICGSTAB method without preconditioning was used to solve the system of equations for the RBF interpolation. Instead of performing an actual matrix-vector multiplication, Eq. (6) is solved during the BICGSTAB iteration. Upon solving Eq. (6), the FMM neighbor list was used to determine the interacting particles. The particles outside the FMM neighbor region were neglected, and the FMM neighbor region was approximately 10σ . The core radius of the vortex elements were set to $2\pi/N$ so that the overlap ratio became $\sigma/dx = 1$. The homogeneity of the present flow field permits the use of a rather small overlap ratio, which allows us to achieve a high spatial resolution using minimum calculation effort.

3.2. Test for $S = 0$

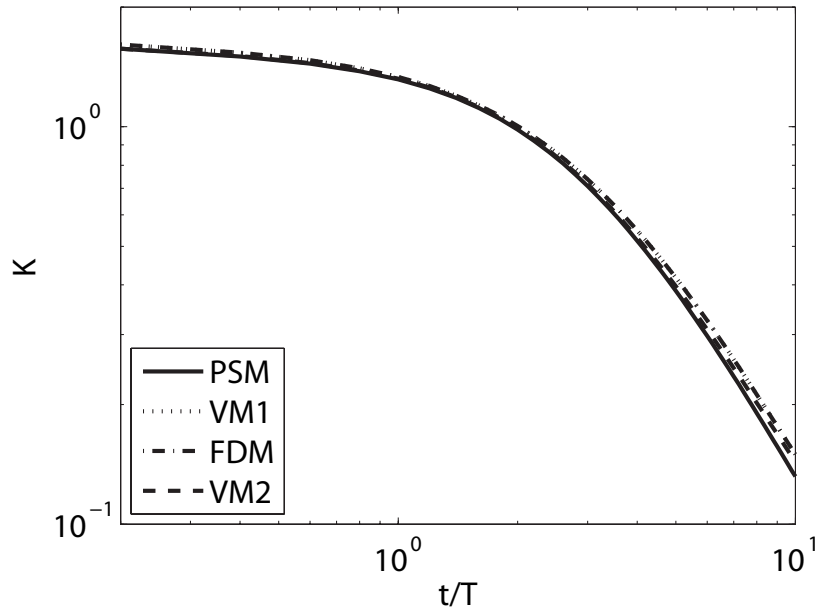
In order to verify the codes used in the present calculation, the isotropic turbulence calculation was performed using the following four codes; the pseudo-spectral method code used in the isotropic turbulence calculation by Yokota *et al.* [9] (PSM), the vortex method code used in the isotropic turbulence calculation (VM1), the present finite difference method code for the homogeneous shear flow with $S = 0$ (FDM), and the present vortex method code for the homogeneous shear flow with $S = 0$ (VM2). The initial Reynolds number was $Re_\lambda = 25$ and the number of calculation points was $N = 64^3$. The time increment was $\Delta t = 0.005$ for all calculations, which corresponds to $t = 0.25\tau$, where τ is the Kolmogorov time scale.

The decay of kinetic energy for the four cases is shown in Fig. 5(a). The results of the two vortex method calculations are almost identical. The difference between the pseudo-spectral method and finite difference method is also very small. The energy spectrum at $t/T = 10$ is shown in Fig. 5(b), where T is the eddy turnover time $T = 0.25$. There is a visible difference between the results of the vortex methods and the grid-based methods. This is considered to be the result of the cumulative errors in the vortex method calculations. However, considering the fact that the Kolmogorov wavenumber is $k_\eta \approx 20$ for this flow, the discrepancies at the higher wavenumbers do not pose a serious problem to the overall kinetic energy balance.

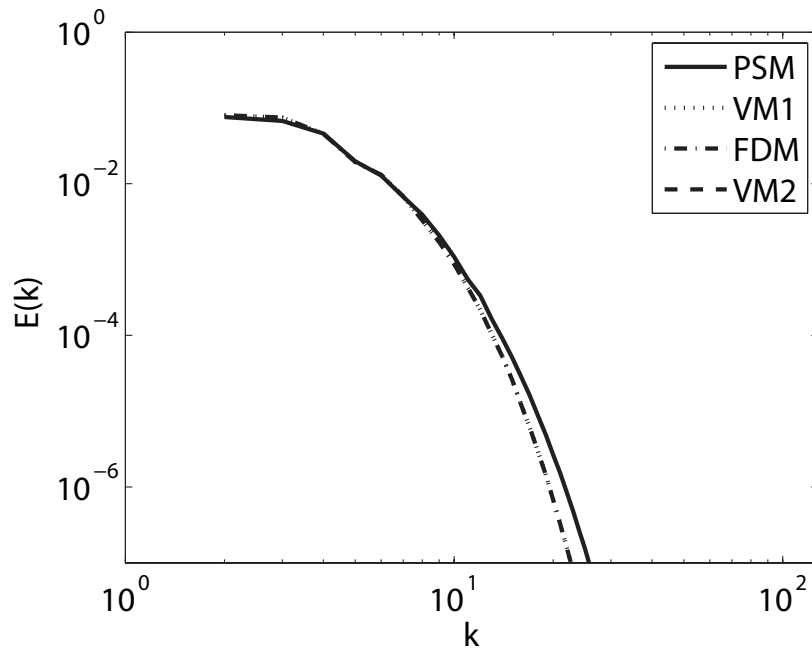
In summary, the pseudo-spectral method, finite difference method, and vortex method produce similar results for the decaying isotropic turbulence. The match in the kinetic energy decay rate indicates the correctness of the present calculation codes.

3.3. Anisotropic structures

One of the main objectives of the present study is to ascertain the magnitude of anisotropy, which the vortex blob method can handle. Lee *et al.* [11] showed in their pseudo-spectral calculation of the homogeneous shear flow, that a high shear-rate produces streaky structures similar to those observed in the near-wall region of the channel flow DNS by Kim *et al.* [16]. They also investigated the suitable turbulence length scale that can be used to construct a dimensionless and universal shear-rate parameter, which can be used as an indicator of streaky structures for both the homogeneous shear flow and high shear regions near the wall.



(a) Decay of Kinetic Energy

(b) Energy Spectrum at $t/T=10$ Figure 5. Isotropic Turbulence Calculation for $Re_\lambda = 25$, $N = 64^3$

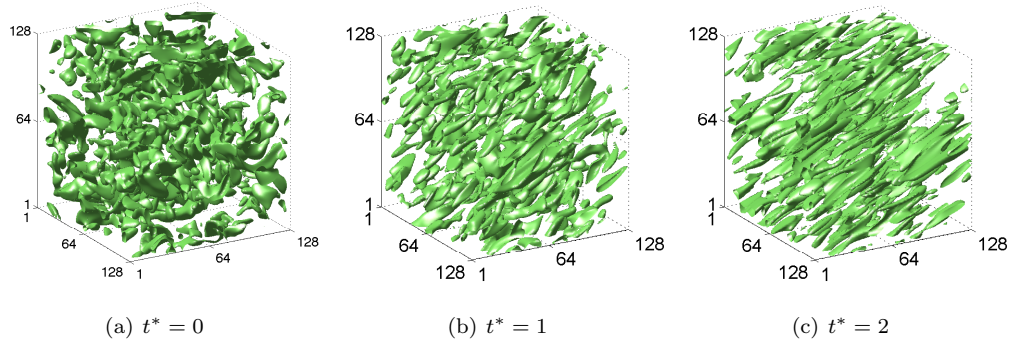


Figure 6. Isosurface of II (Finite Difference Method)

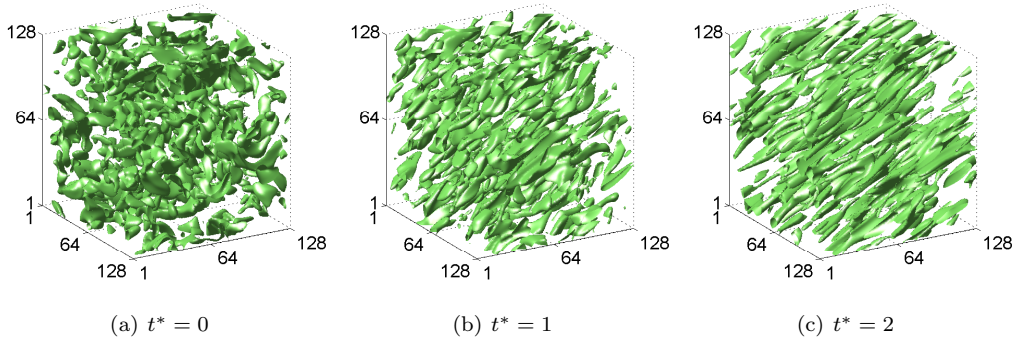


Figure 7. Isosurface of II (Vortex Method)

This dimensionless shear-rate parameter is defined as

$$S^* \equiv \frac{2SK}{\epsilon} \quad (13)$$

where $K = \overline{u_i^2}/2$ is the turbulent kinetic energy and $\epsilon = \nu \overline{u_{i,j} u_{j,i}}$ is the dissipation rate. Lee *et al.* [11] applied this shear-rate parameter to the fully developed channel flow by Kim *et al.* [16] and showed that the maximum is $S^* = 35$ in the viscous sublayer, and decreases to about one-sixth of the maximum in the logarithmic layer. In the present calculation the shear-rate $S = 18$ is chosen so that the shear-rate parameter becomes $S^* \approx 35$.

We will first present the qualitative aspects of the present calculations. The isosurface of the second invariant of the velocity gradient tensor $II = u_{i,j} u_{j,i}$ for the finite difference method and vortex method are shown in Figs. 6 and 7, respectively. The time t^* is normalized by the shear-rate S . At $t^* = 0$, the flow is isotropic and the structures have no directional preference. At $t^* = 1$, the vortices are strained and the structures begin to show a directional preference. At $t^* = 2$, many streaky structures can be observed. From these results, it has been confirmed that the vortex method can reproduce the streaky structures in high shear flows very well.

3.4. Anisotropy tensors

The anisotropy tensor of the Reynolds stress

$$b_{ij} = \frac{\overline{u_i u_j}}{\overline{u_k u_k}} - \frac{1}{3} \delta_{ij}. \quad (14)$$

is a direct measure of the anisotropy of the velocity fluctuations, and is a more quantitative measure of the ability to reproduce anisotropic turbulence. The normal components of the Reynolds stress anisotropy tensor are shown in Fig. 8, while the non-normalized Reynolds stresses are shown in Fig. 9. FDM(64^3), VM(64^3), FDM(128^3), and VM(128^3) are the finite difference method using a $N = 64^3$ grid, the vortex method using $N = 64^3$ particles, the finite difference method using a $N = 128^3$ grid, and the vortex method using $N = 128^3$ particles. Different markers represent the different normal components. The overall behavior of the present vortex method is similar to that of the finite difference method. The results of the two finite difference method calculations are indistinguishable. On the other hand, when the spatial resolution of the vortex method is increased, the difference between the finite difference method and vortex method decreases. This suggests that the discretization error of the finite difference method at $N = 64^3$ is small enough to remain undetected, while the discretization error of the vortex method at $N = 64^3$ is clearly observed. Although both methods converge to the same results for larger N , the discretization error for a given N seems to be larger for vortex methods, which is consistent with the observations in the isotropic turbulence calculations [9].

From these observations, it can be said that the present vortex method code can account for strong anisotropy comparable to that in the viscous sublayer of a near wall flow if the spatial resolution is sufficient. Though, the number of necessary vortex elements may be large compared to grid-based methods. This is evident from the fact that the results of the finite difference method for two different spatial resolutions match, while the results of the vortex method for two different spatial resolutions do not.

3.5. Reynolds shear stress

The probability density function (PDF) of the Reynolds shear stress $u_1 u_3$ is shown for several time steps in Fig. 10. The probability density for the product $x = u_1 u_3 / \langle u_1 u_3 \rangle$ of two jointly Gaussian distributions with zero mean is given by

$$P_{u_1 u_3}(x) = \frac{|r|}{\pi \sqrt{1 - r^2}} \exp \left(\frac{r^2 x}{1 - r^2} \right) K_0 \left(\left| \frac{rx}{1 - r^2} \right| \right) \quad (15)$$

where $r = \langle u_1 u_3 \rangle / \sigma_{u_1} \sigma_{u_3}$ is the correlation coefficient and K_0 is the zeroth order modified Bessel function of the second kind [17]. The solid line corresponds to the PDF of $(x - \langle x \rangle) / \sigma_{x - \langle x \rangle}$, while the dashed line represents the Gaussian joint PDF calculated from Eq. 15. FDM and VM are the results of the finite difference method and vortex method both using $N = 128^3$ calculation points. The PDF of the solid line is slightly larger than that of the dashed line at the tails. This is caused by the non-Gaussian distribution of the velocity, and has been reported in previous calculations [18]. The results of the finite difference method and vortex method seem, at first glance, quite similar. However, at $t^* = 4$ the PDF of the vortex method is close to the joint Gaussian fit, whereas the PDF of the finite difference method remains non-Gaussian.

We have observed that the discretization error for a given number of calculation points seems to be larger for vortex methods. The Gaussian basis function used in the present vortex method

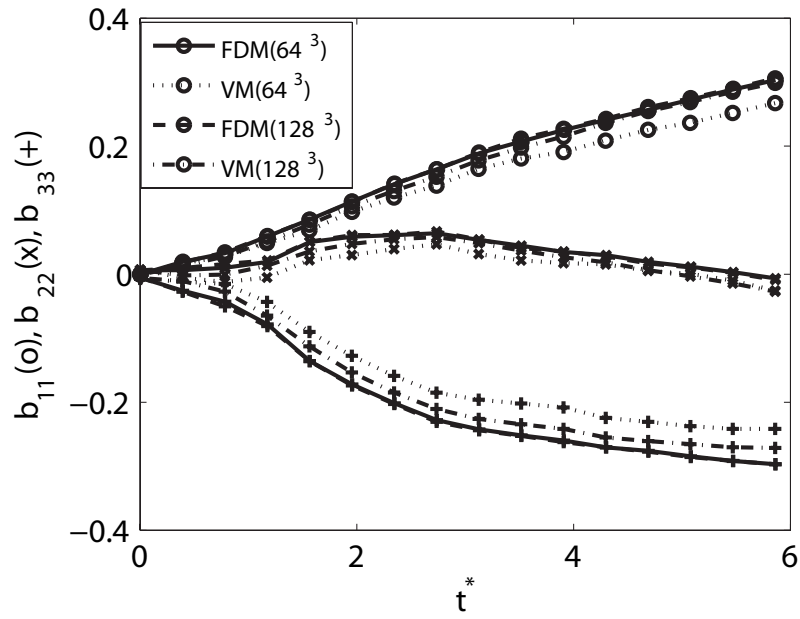


Figure 8. The Development of the normal components of the Reynolds Stress Anisotropy Tensor

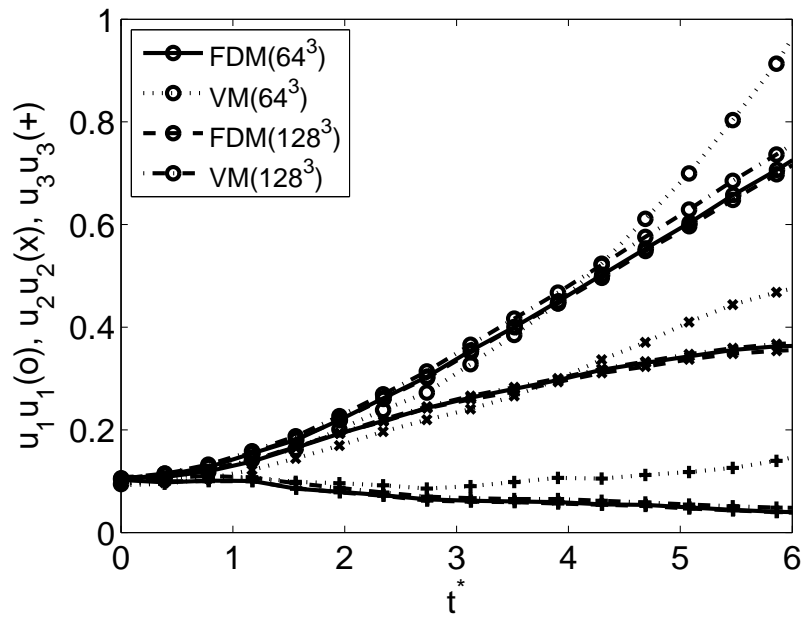


Figure 9. The Development of the normal components of the Reynolds Stress

calculations is of second order. From the results of the present calculations, it is suggested that fourth order basis functions [3] are necessary to compete with fourth order finite difference methods in terms of the spatial discretization error. This is especially so if we consider the fact that most finite difference methods used for the direct numerical simulation of turbulence are fourth order or higher.

We will take a closer look at the correlation between u_1 and u_3 by examining the joint PDF in Fig. 11. The isoprobability contours are logarithmically spaced, and are separated by factors of 10. A strong negative correlation is observed in both the FDM and VM. The shapes of the third and fourth contour lines from the center are slightly different, which is consistent with the difference observed in the previous $P(u_1 u_3)$ plots. The skewness and flatness of $u_1 u_3$ are $S_{FDM} = -4.87$, $F_{FDM} = 26.3$, and $S_{VM} = -4.92$, $F_{VM} = 25.4$ for the finite difference method and vortex method, respectively.

In Fig. 12 the PDF of ω_1 , ω_2 and ω_3 at $t^* = 4$ are shown. The dashed curve represents the Gaussian distribution. The streamwise vorticity ω_1 remains symmetric, but the spanwise component ω_2 and transverse component ω_3 are skewed toward the positive direction. Furthermore, for ω_2 the negative side is steeper than the Gaussian distribution and the positive side is flatter. The asymmetry of the PDF of ω_2 reflects the generation of vorticity in the positive direction due to the mean shear. ω_3 matches the Gaussian distribution near the origin, but deviates from the Gaussian at the tails. These characteristics are similar to the observations made by Kida & Tanaka [19] in their pseudo-spectral method calculation. The PDFs of vorticity shown in Fig. 12 show a close resemblance between the finite difference method and vortex method.

From these observations we conclude that both the instantaneous and statistical features of the anisotropy are accurately calculated in the present vortex method. Our argument that the vortex method can reproduce globally anisotropic structures using locally isotropic elements has been supplemented from a statistical viewpoint by confirming the reproducibility of the global non-Gaussian turbulence using elements with local Gaussian smoothing.

3.6. Energy spectrum equation

The remaining objective of the present investigation is the quantitative assessment of the ability of vortex methods to calculate the balance between production, transfer, and dissipation in the homogeneous shear flow. Since the production was not present in the isotropic turbulence, its quantitative assessment is of interest for the present homogeneous shear calculation.

The energy spectrum equation for the homogeneous shear flow can be written as

$$\frac{\partial K}{\partial t} = \underbrace{Sk_1 \frac{\partial K}{\partial k_3}}_{\mathcal{P}} - \underbrace{\mathcal{E}_{13}}_{\mathcal{T}} + \underbrace{\iota k_k \mathcal{T}_{ik,i}}_{\mathcal{T}} - \underbrace{2\nu k^2 K}_{\epsilon} \quad (16)$$

where \mathcal{E}_{ij} and $\mathcal{T}_{ij,k}$ are the two point double and triple velocity correlation tensors in wavenumber space, respectively [20]. K is the kinetic energy $K \equiv \frac{1}{2} \mathcal{E}_{ii}$, S is the shear-rate defined in Eq. (3), k is the wavenumber, and ν is the kinematic viscosity. Each term on the right hand side of Eq. (16) is associated with an actual physical process. \mathcal{P} represents the production, \mathcal{T} represents the transfer, and ϵ represents the dissipation of the kinetic energy.

The budget of the above mentioned energy spectrum equation at $t^* = 2$ for the finite difference method and vortex method is shown in Fig. 13. Although there are quantitative

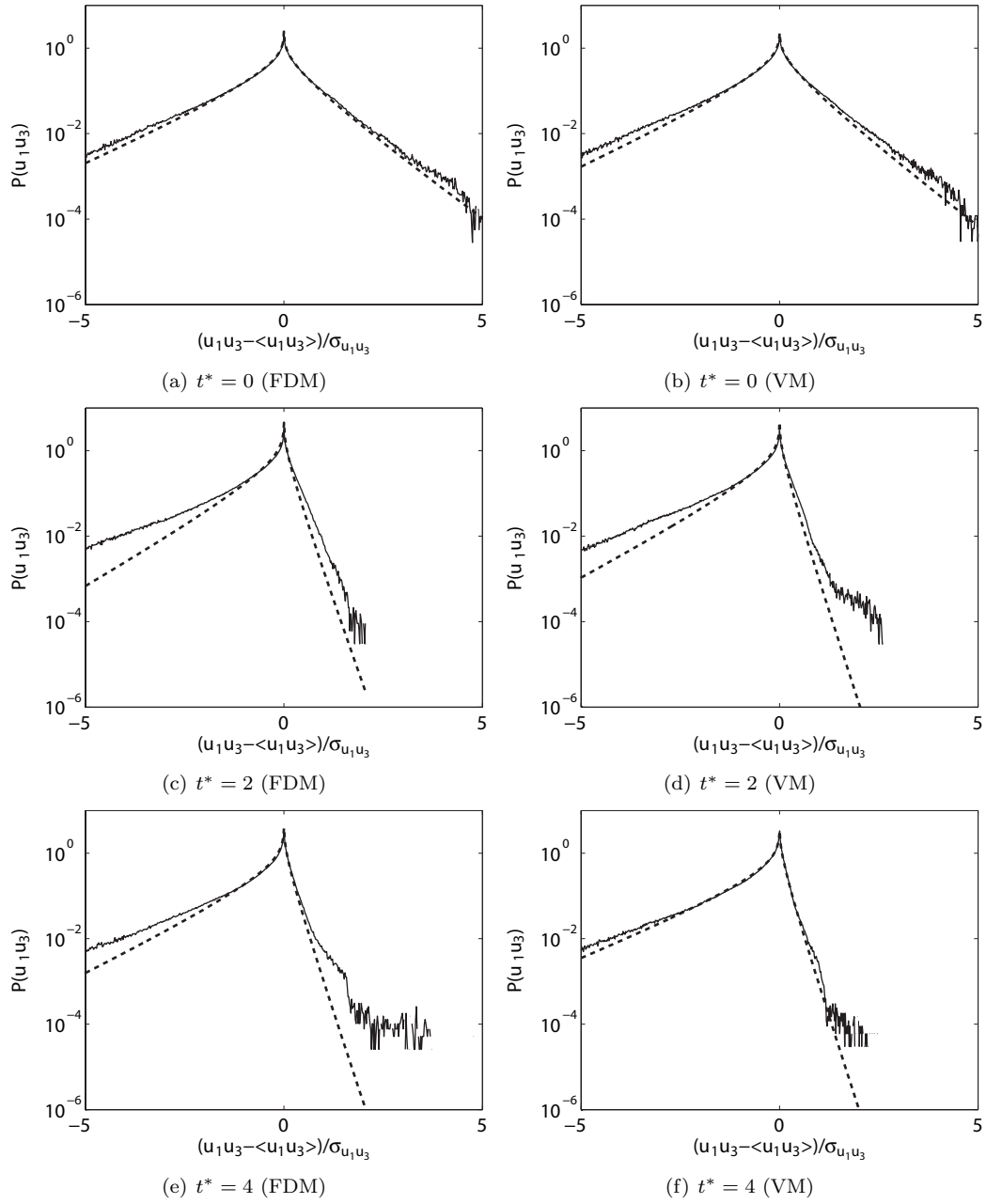
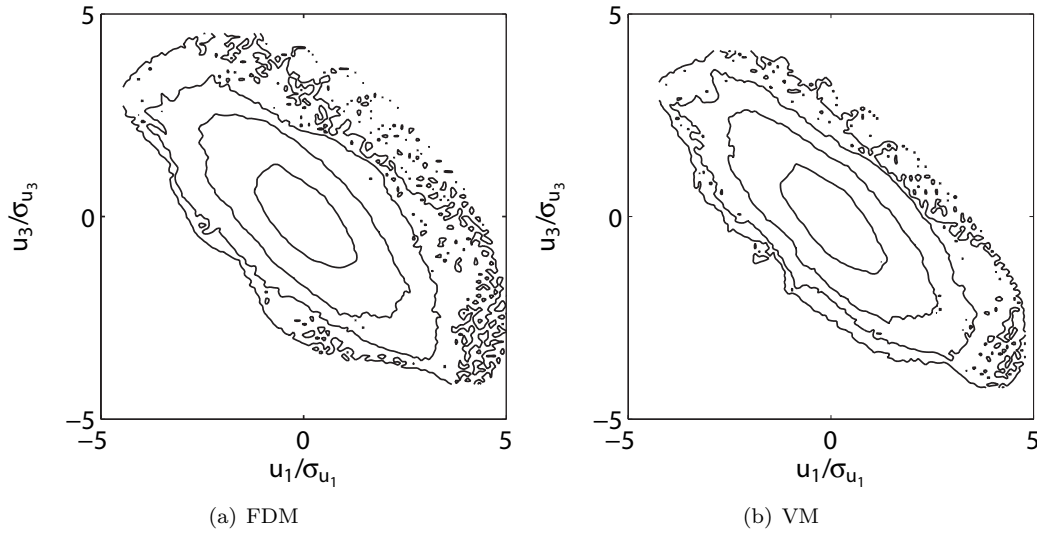


Figure 10. PDF of u_1u_3 . Solid lines correspond to the PDF of $(x - \langle x \rangle)/\sigma_{x - \langle x \rangle}$. Dashed lines represent the Gaussian joint PDF calculated from Eq. (15).

Figure 11. Joint PDF of u_1 and u_3 at $t^* = 4$

differences in the two plots, the overall tendency is very similar. First, the production has a peak at lower wavenumbers and vanishes at higher wavenumbers. This corresponds to the fact that the mean shear mainly influences the large structures of turbulence. Secondly, the transfer term has a large negative value at lower wavenumbers and has a positive value at higher wavenumbers. This reflects the fact that the energy drawn from the larger structures is gradually cascaded down to the smaller structures. Furthermore, the dissipation term has a negative peak at higher wavenumbers, although not too high for the present calculation at $Re_\lambda = 25$. Finally, the change rate of kinetic energy shows an energy surplus, which is consistent with the fact that the total kinetic energy increases over time.

3.7. Production of enstrophy and strain

The turbulent dynamical quantities which have direct impacts on energy cascade and turbulent energy dissipation are the strain production $-S_{ij}S_{jk}S_{ki}$ and enstrophy production $\omega_i\omega_jS_{ij}$. The strain production is a local self-amplification process, which contributes positively to the transport equation of the total strain. The enstrophy production is associated with the vortex stretching process, and acts as a source in the transport equation of enstrophy but acts as a sink in the transport equation of the total strain. The correlation of these values is a direct measure for evaluating the process of strain production, vortex stretching, and strain destruction.[21]

The joint PDFs of $-S_{ij}S_{jk}S_{ki}$ and $\omega_i\omega_jS_{ij}$ for $t^* = 0$, $t^* = 2$, and $t^* = 4$ are shown in Fig. 14. The initial condition of the present calculations is a homogeneous isotropic turbulence, and both the strain production and enstrophy production are skewed heavily towards the positive side at $t^* = 0$. However, there is no particular correlation between the two at this point. At $t^* = 2$ the skewness of the individual PDFs decrease and the correlation between them increase. At $t^* = 4$ this tendency becomes even clearer. The results of the finite difference method and vortex method a

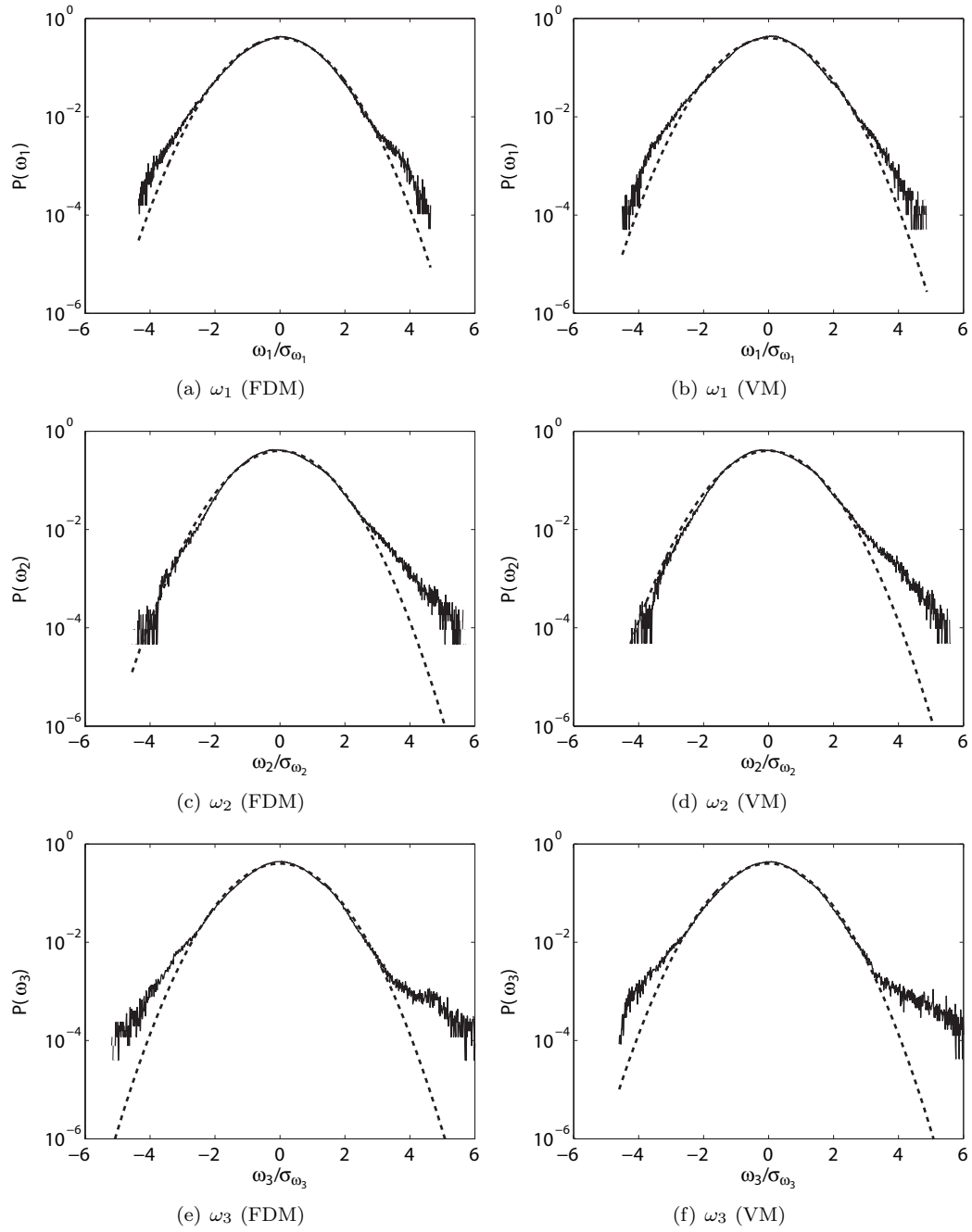
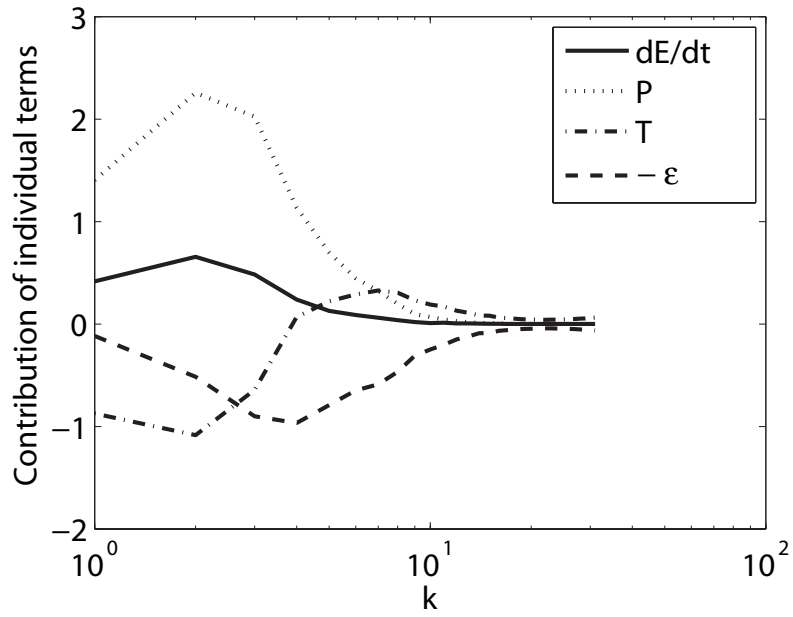
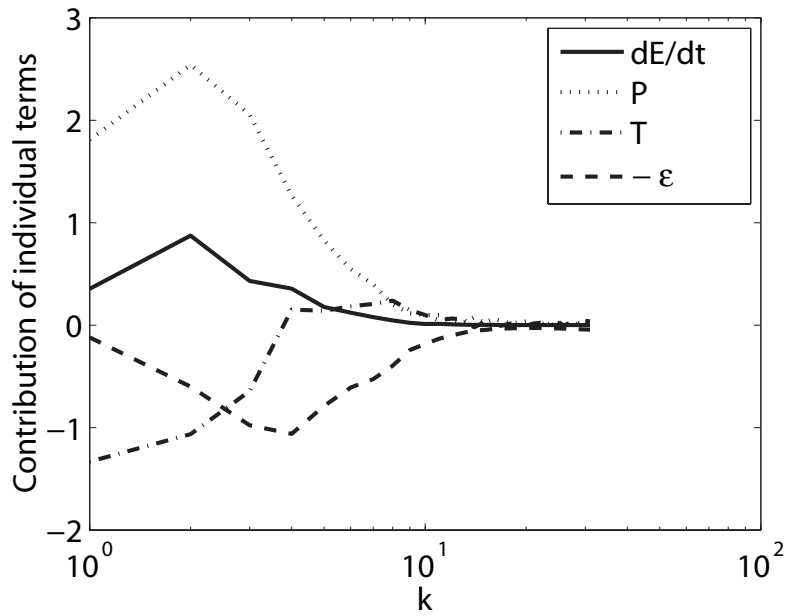


Figure 12. PDF of ω_1 , ω_2 and ω_3 at $t^* = 4$. Solid lines represent the PDF of vorticity, while the dashed lines represent the Gaussian distribution for the same domain.



(a) FDM



(b) VM

Figure 13. Budget of the Energy Spectrum Equation at $t^* = 2$

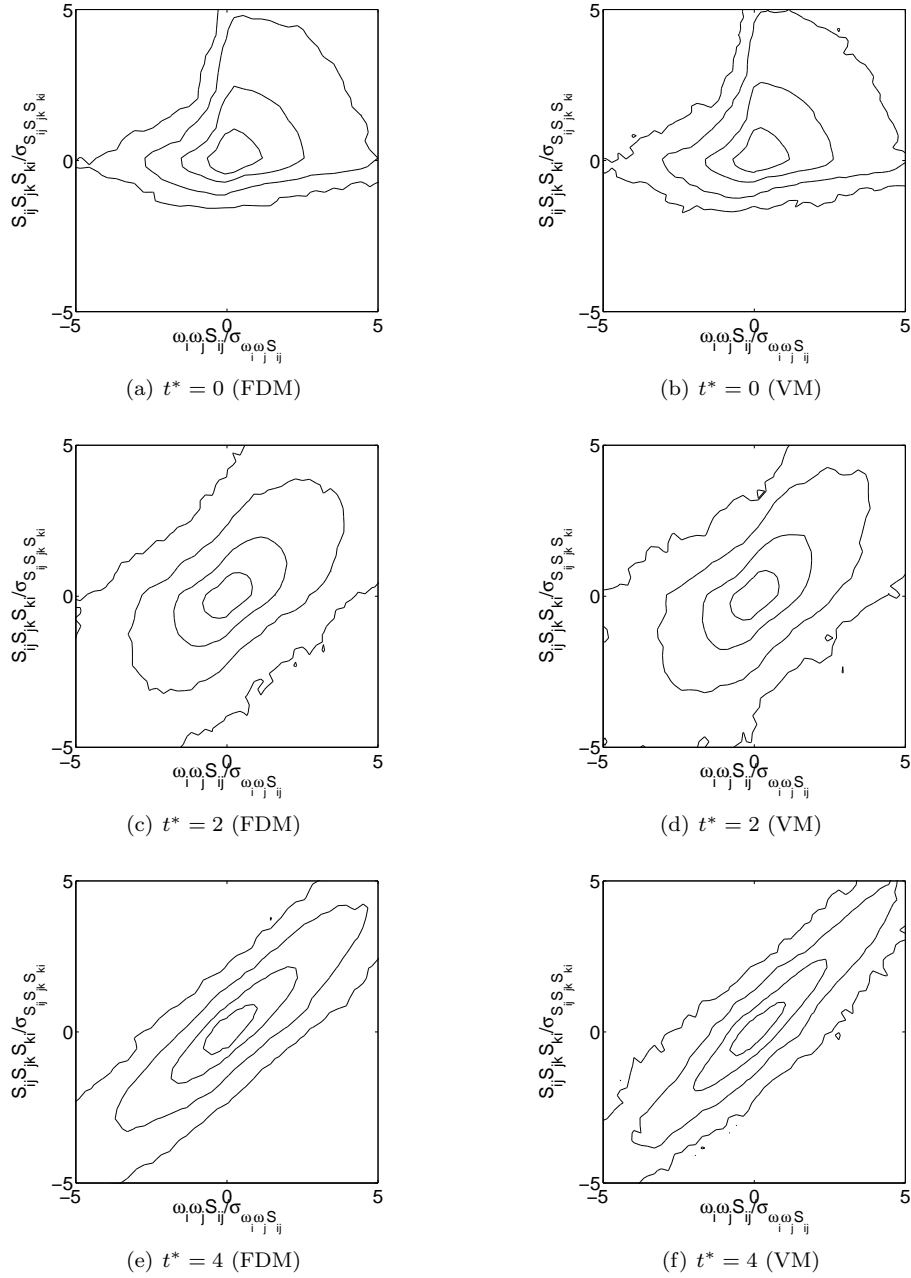


Figure 14. PDF of ω_1 , ω_2 and ω_3 at $t^* = 4$. Solid lines represent the PDF of vorticity, while the dashed lines represent the Gaussian distribution for the same domain.

4. CONCLUSIONS

The FMM has been extended to periodic boundary conditions with shear. Using this shear periodic FMM, the core-spreading vortex method with spatial adaptation has been applied to the calculation of a homogeneous shear turbulence, and compared with a finite difference code under identical calculation conditions.

The asymptotic behavior of the error in the present shear periodic FMM is identical to that of the periodic FMM without shear. The increase in CPU-time caused by the additional calculation of the $16 \times 16 \times 16$ shear periodic image cells is approximately 30% of the total CPU-time of the shear periodic FMM.

The vortical structures observed in the isosurface plots of the second invariant of the velocity derivative tensor were in good accordance between the two methods. The anisotropy of the Reynolds stress shows that the present vortex method can quantitatively match the results of the finite difference method if the spatial resolution is sufficient. Using isotropic vortex blobs does not prevent the vortex method from accurately calculating anisotropic turbulence, because the flow is, to some extent, locally isotropic.

The agreement between the finite difference method and vortex method for the probability density functions shows that the vortex method reproduces the statistical aspects of the strongly sheared turbulence, accurately. Furthermore, the budget of the energy spectrum equation shows that the details of the energy transfer are also properly calculated in the present vortex method.

From these observations, we conclude that the present vortex method is valid for solving flows with a shear-rate parameter of $S^* \approx 35$, which is equal to the maximum value observed in a fully developed channel flow. This allows us to rule out the possibility of any detrimental effects caused by the mean shear, when validating the vortex method for near-wall flows in the future.

In summary, the present comparison between finite difference methods and vortex methods suggests that vortex methods can be used for the direct numerical simulation of highly sheared turbulence. However, it has also been confirmed that the relative inefficiency of the spatial discretization of vortex methods has a significant impact on the results of the simulation, and the use of higher-order basis functions are recommended in future simulations.

REFERENCES

1. Sbalzarini IF, Walther JH, Bergdorf M, Hieber SE, Kotsalis EM, Koumoutsakos P. PPM-A highly efficient parallel particle-mesh library for the simulation of continuum systems. *Journal of Computational Physics* 2006; **215**:566–588.
2. Poncet P. Finite difference stencils based on particle strength exchange schemes for improvement of vortex methods. *Journal of Turbulence* 2006; **7**(23):1–24.
3. Rossi LF. Achieving high-order convergence rates with deforming basis functions. *SIAM Journal on Scientific Computing* 2005; **26**(3):885–906.
4. Ploumhans P, Daeninck G, Winckelmans G. Simulation of three-dimensional bluff-body flows using the vortex particle and boundary element methods. *Flow, Turbulence and Combustion* 2004; **73**(2):117–131.
5. Barba LA, Leonard A, Allen CB. Advances in viscous vortex methods- Meshless spatial adaption based on radial basis function interpolation. *International Journal for Numerical Methods in Fluids* 2005; **47**(5):387–421.
6. Eldredge JD, Leonard A, Colonius T. A general deterministic treatment of derivatives in particle methods. *Journal of Computational Physics* 2002; **180**:686–709.

7. Winckelmans GS, Leonard A. Contributions to vortex particle methods for the computation of three-dimensional incompressible unsteady flows. *Journal of Computational Physics* 1993; **109**:247–273.
8. Totsuka Y, Obi S. The vortex method applied to simulation of homogeneous isotropic turbulence. *International Conference on Computational Methods*, Singapore, Dec. 15-17, 2004; FP212.
9. Yokota R, Sheel TK, Obi S. Calculation of isotropic turbulence using a pure Lagrangian vortex method. *Journal of Computational Physics* 2007; **226**:1589–1606.
10. Cottet GH, Michaux B, Ossia S, VanderLinden G. A comparison of spectral and vortex methods in three-dimensional incompressible flows. *Journal of Computational Physics* 2002; **175**:702–712.
11. Lee MJ, Kim J, Moin P. Structure of turbulence at high shear rate. *Journal of Fluid Mechanics* 1990; **216**:561–583.
12. Lambert CG, Darden TA, Board JA. A multipole based algorithm for efficient calculation of forces and potentials in macroscopic periodic assemblies of particles. *Journal of Computational Physics* 1996; **126**:274–285.
13. Schumann U. Algorithms for direct numerical simulation of shear-periodic turbulence. *Lecture Notes in Physics* 1985; **218**.
14. Rogallo RS. Numerical experiments in homogeneous turbulence. NASA TM-81315, 1981.
15. Williamson JH. Low-storage Runge-Kutta schemes. *Journal of Computational Physics* 1980; **35**:48–56.
16. Kim J, Moin P, Moser RD. Turbulence statistics in fully developed channel flow at low Reynolds number. *Journal of Fluid Mechanics* 1987; **177**:133–166.
17. Lu SS, Willmarth WW. Measurements of the structure of the Reynolds stress in a turbulent boundary layer. *Journal of Fluid Mechanics* 1973; **60**:481–511.
18. Pumir A. Turbulence in homogeneous shear flows. *Physics of Fluids* 1996; **8**:3112–3127.
19. Kida S, Tanaka M. Reynolds stress and vortical structure in a uniformly sheared turbulence. *Journal of the Physical Society of Japan* 1992; **61**:4400–4417.
20. Bernard PS, Wallace JM. *Turbulent Flow*. John Wiley & Sons, 2002.
21. Guala M, Liberzon A, Tsinober A, Kinzelbach W. An experimental investigation on Lagrangian correlations of small-scale turbulence at low Reynolds number. *Journal of Fluid Mechanics* 2007; **574**:405–427.